Regularized deconvolution method for turbulent combustion modeling

By Q. Wang, H. Wu AND M. Ihme

1. Motivation and objectives

Large-eddy Simulation (LES) of turbulence combustion introduces difficulties that are associated with the representation of the turbulence-chemistry interaction, occurring on numerically unresolved scalars. Combustion models that rely on reaction transport manifolds, such as Intrinsic Low Dimensional Manifold, Flame Prolongation in ILDM (Gicquel *et al.* 2000), Flamelet Generated Manifold (Oijen & Goey 2000), Flamelet Progress Variable (Pierce & Moin 2004), have been developed. In these models, the thermochemical state is represented in terms of a reduced set of scalars, and the turbulence-chemistry interaction is considered through a presumed PDF closure. While this approach is effective in reducing the computational complexity of the simulation, these models rely on intrinsic assumptions about the asymptotic flame structure. Therefore, the accuracy of these models deteriorates when they are applied in other regimes. However, combustion applications often involve multi-regimes. To account for this issue, Wu *et al.* (2015) developed a Pareto-efficient Combustion (PEC) model the provides an optimal sub-model selection to ensure model compliance with the underlying flow field representation.

To couple the chemistry models with turbulence, a turbulence closure is required. Flamelet based combustion models typically considers the asymptotic regimes of premixed and diffusion flames. Topology-dependent the turbulence closure are developed for these models, such as the Filtered Tabulated Chemistry Model for LES (Fiorina *et al.* 2009) for premixed flames and presumed PDF closure for non-premixed flames (Ihme *et al.* 2005). Topology-free closures, such as the transported PDF (Pope 1985) and the Linear Eddy Model (Kerstein 1988) resolve this issue but they are typically computationally more expensive. To extend the flamelet models to multi-regime environments, there is a need to develop new turbulence closures that are independent of an underlying flame topology.

To address this need, turbulent closures using deconvolution method are considered. The deconvolution method is an approximate inverse to the filter operation in LES. Consequently, the sub-grid scale (SGS) terms in the LES-equations can be computed explicitly using the deconvolved scalars. Since no assumptions on the reconstructed flow field are made in deriving the deconvolution operator, this approach has the potential to be independent of an underlying flame topology and therefore it is applicable as sub-grid model for flamelet methods.

The deconvolution method was first introduced in LES of non-reactive flows as a closure for the SGS stress term (Stolz & Adams 1999), and the method was tested on different flow configurations (Stolz *et al.* 2001*b*,*a*; Schlatter *et al.* 2004). The application of the deconvolution method to reactive LES was formulated by Pantano & Sarkar (2001) and Mellado *et al.* (2003) using a moment-based reconstruction of the scalar field. An approximate deconvolution operator derived from a Taylor-series expansion to the

Gaussian filter was developed by Domingo & Vervisch (2015), and model was successfully validated on a turbulent Bunsen flame.

Deconvolution operators that are developed for LES are all linear operators. Despite their simplicity in implementation, there are two major drawbacks that are common to all linear deconvolution operators, namely, the lack of boundedness and conservation properties of scalars. In non-reacting LES, the deconvolution operation is applied to velocities, for which these issues are not important since there are no constraints on the value of velocity. However, due to the constraints of reactive scalar mass fraction which are strictly bounded and total species mass is conserved at all time, these two issues becomes critical in combustion LES modeling. To address these issues, a regularized deconvolution method is developed. This method ensures both constraints by formulating the deconvolution operator as solution to an minimum mean square error (MMSE) optimization problem (Section 2). The method is examined in an *a priori* study to qualify the accuracy in both scalar reconstruction and turbulent chemical source term closure computation (Section 4).

2. Deconvolution methods

Deconvolution models are used as closures for explicit LES. A summary of the mathematically formulations are provided. Denoting $G(\boldsymbol{x})$ as the time invariant filter kernel in physical space, the explicit filtering of scalar $\phi(\boldsymbol{x},t)$ is given by the following convolution operation:

$$\overline{\phi}(\boldsymbol{x},t)=\int_{-\infty}^{\infty}G(\boldsymbol{x}-\boldsymbol{x'})\,\phi(\boldsymbol{x'},t)\,d\boldsymbol{x'}=:G*\phi, \tag{2.1}$$

and the Favre filtering has the form

$$\widetilde{\phi}(\boldsymbol{x},t)=\frac{\int_{-\infty}^{\infty}G(\boldsymbol{x}-\boldsymbol{x'})\,\rho(\boldsymbol{x'},t)\,\phi(\boldsymbol{x'},t)\,d\boldsymbol{x'}}{\int_{-\infty}^{\infty}G(\boldsymbol{x}-\boldsymbol{x'})\,\rho(\boldsymbol{x'},t)\,d\boldsymbol{x'}}=:\widetilde{G}*\phi. \tag{2.2}$$

With this, the deconvolution operations can be derived as follows. Denoting Q as the deconvolution kernel in physical space, the deconvolution operation to the filtered scalar $\overline{\phi}(\boldsymbol{x},t)$ is given by

$$\phi^{D}(\boldsymbol{x},t)=\int_{-\infty}^{\infty}Q(\boldsymbol{x}-\boldsymbol{x'})\,\overline{\phi}(\boldsymbol{x'},t)\,d\boldsymbol{x'}=:Q*\bar{\phi}, \tag{2.3}$$

where ϕ^{D} is the deconvolved scalar. Accordingly, the Favre deconvolution takes the form

$$\phi^{\widetilde{D}}(\boldsymbol{x},t)=\frac{\int_{-\infty}^{\infty}Q(\boldsymbol{x}-\boldsymbol{x'})\,\overline{\rho}(\boldsymbol{x'},t)\,\widetilde{\phi}(\boldsymbol{x'},t)\,d\boldsymbol{x'}}{\int_{-\infty}^{\infty}Q(\boldsymbol{x}-\boldsymbol{x'})\,\overline{\rho}(\boldsymbol{x'},t)\,d\boldsymbol{x'}}=:\widetilde{Q}*\phi. \tag{2.4}$$

The deconvolved scalar is an approximation of the unfiltered scalar. Depending on the filter type, we have $\phi\approx\phi^{D}$ for Reynolds filtered scalars and $\phi\approx\phi^{\widetilde{D}}$ for Favre filtered scalars.

2.1. *Approximate Deconvolution Method (ADM)*

A commonly used approach to deconvolution is the van Cittert filter (Layton & Rebholz 2012), which is defined by an iterative expression:

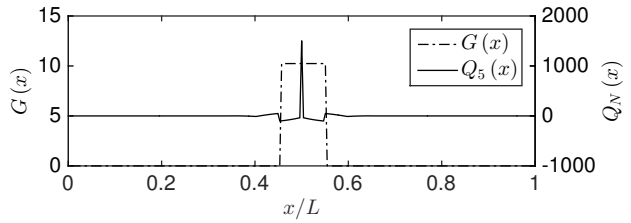

FIGURE 1. Box filter (dotted line) and the ADM deconvolution operator with $N = 5$ (solid line) for filter width of $0.1L$ in physical space.

$$\phi^{(\nu+1)} = \phi^{(\nu)} + \left(\bar{\phi} - G * \phi^{(\nu)}\right), \tag{2.5}$$

where ν is the number of iterations. The deconvolution operator can be derived recursively from the van Cittert filter as

$$Q_N := \sum_{\nu=0}^{N} (I - G)^{\nu}. \tag{2.6}$$

By using a finite N this method is referred to as the Approximate Deconvolution Method (ADM) (Stolz & Adams 1999). Figure 1 shows an example of the ADM operator with $N = 5$. The test filter in Figure 1 is a box filter with filter width $\Delta = 0.1L$ in physical domain. The operator for $N = 5$ is bandwidth limited. However, as N increases, both the bandwidth and the amplitude of Q_N grows. Practically, $N = 5$ is used in LES.

2.2. *Wiener filter*

The Wiener filter is obtained as solution to the Minimum Mean Square Error (MMSE) optimization problem. By considering the Fourier solution to ϕ, the MMSE problem can be written as

$$\min_{\hat{\phi}(\boldsymbol{\kappa},t)^D} \mathrm{E}\left\{\left|\hat{\phi}(\boldsymbol{\kappa},t) - \hat{\phi}^D(\boldsymbol{\kappa},t)\right|^2\right\}, \tag{2.7}$$

where $\hat{\phi}$ is the scalar in Fourier space and $\hat{\phi}^D(\boldsymbol{\kappa},t) = \hat{Q}(\boldsymbol{\kappa})\,\overline{\hat{\phi}}(\boldsymbol{\kappa},t)$ is the deconvolved scalar in Fourier space. Assuming the filtered signal in the form $\overline{\hat{\phi}}(\boldsymbol{\kappa},t) = \hat{G}(\boldsymbol{\kappa})\,\hat{\phi}(\boldsymbol{\kappa},t) + \hat{n}(\boldsymbol{\kappa},t)$, where $\hat{n}(\boldsymbol{\kappa},t)$ is the noise, let $\epsilon(\boldsymbol{\kappa},t) = \mathrm{E}\left\{\left|\hat{\phi}(\boldsymbol{\kappa},t) - \hat{\phi}^D(\boldsymbol{\kappa},t)\right|^2\right\}$, upon taking the derivative of $\epsilon(\boldsymbol{\kappa},t)$ with respect to $\hat{Q}(\boldsymbol{\kappa})$ and equating it to zero, the following solution to the MMSE problem is obtained:

$$\hat{Q}(\boldsymbol{\kappa}) = \frac{\hat{G}^*(\boldsymbol{\kappa})\,\hat{S}(\boldsymbol{\kappa},t)}{\left|\hat{G}(\boldsymbol{\kappa})\right|^2 \hat{S}(\boldsymbol{\kappa},t) + \hat{N}(\boldsymbol{\kappa},t)}, \tag{2.8}$$

where

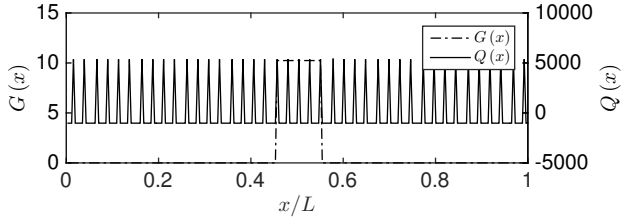

FIGURE 2. Box filter (dotted line) and the MMSE deconvolution operator (solid line) for filter width of $0.1L$ in physical space.

$$\hat{S}(\boldsymbol{\kappa},t) = \mathrm{E}\left\{\left|\hat{\phi}(\boldsymbol{\kappa},t)\right|^2\right\} = \left\langle\left|\hat{\phi}(\boldsymbol{\kappa},t)\right|^2\right\rangle; \tag{2.9a}$$

$$\hat{N}(\boldsymbol{\kappa},t) = \mathrm{E}\left\{\left|\hat{n}(\boldsymbol{\kappa},t)\right|^2\right\} = \left\langle\left|\hat{n}(\boldsymbol{\kappa},t)\right|^2\right\rangle, \tag{2.9b}$$

are the ensemble averages of the power density function of the signal and noise respectively.

For a non-trivial signal, $\hat{S}(\boldsymbol{\kappa},t)$ in equation (2.8) can be eliminated from both the numerator and the denominator, which results in the following form of the deconvolution model:

$$\hat{Q}(\boldsymbol{\kappa}) = \frac{\hat{G}^*(\boldsymbol{\kappa})}{\left|\hat{G}(\boldsymbol{\kappa})\right|^2 + \eta(\boldsymbol{\kappa},t)}, \tag{2.10}$$

where $\eta(\boldsymbol{\kappa},t) = \hat{N}(\boldsymbol{\kappa},t)/\hat{S}(\boldsymbol{\kappa},t)$ is the inverse of the signal-to-noise ratio; η can be estimated based on knowledge of the spectral property of the problem. In the current model, $\eta(\boldsymbol{\kappa},t)$ is assumed to be constant.

In LES, filtering and deconvolution is conducted in physical space. The MMSE deconvolution operator is inverted back to the physical domain through an inverse Fourier transform. Figure 2 illustrates the deconvolution operator for the box filter function that was also considered in Figure 1 in physical space. Different from the exact filter inversion, the amplitude of the Wiener filter is finite, so that the inversion operation is well defined.

2.3. *Regularized Deconvolution Method (RDM)*

To address the problem of boundedness, inequality constraints to the classical MMSE problem are added, so that Eq. (2.7) can be written as:

$$\begin{array}{ll} \min\limits_{\hat{\phi}^D(\boldsymbol{\kappa},t)} & \mathrm{E}\left\{\left|\hat{\phi}(\boldsymbol{\kappa},t) - \hat{\phi}^D(\boldsymbol{\kappa},t)\right|^2\right\} \\ s.t. & \phi^- \le \phi^D \le \phi^+ \end{array} \tag{2.11}$$

with ϕ^- and ϕ^+ correspond to the lower and upper limits of the scalar. An equivalent optimization problem to Eq. (2.11) in physical space is then given as:

$$\begin{array}{ll} \min\limits_{\phi^D(\boldsymbol{x},t)} & \left\|\bar{\phi}(\boldsymbol{x},t) - G(\boldsymbol{x}) * \phi^D(\boldsymbol{x},t)\right\|_2^2. \\ s.t. & \phi^- \le \phi^D \le \phi^+ \end{array} \tag{2.12}$$

The optimization problem shown in Eq. (2.12) can be solved numerically using a reflective Newton method (Coleman & Li 1996).

To ensure scalar conservation properties, an additional objective function can be added to the MMSE optimization problem:

$$\epsilon_{\phi^D_{tot}} = \int_\Omega \left(\phi^D - \bar{\phi}\right) d\boldsymbol{x} \tag{2.13}$$

where Ω is the computational domain. The implementation is done by including the minimization of the error defined in Eq. (2.13) to the constrained MMSE problem, resulting in the following discrete form:

$$\begin{array}{cc} \min\limits_{\phi^D(\boldsymbol{x},t)} & \left\|\bar{\phi}\left(\boldsymbol{x},t\right) - G\left(\boldsymbol{x}\right) * \phi^D\left(\boldsymbol{x},t\right)\right\|_2^2 + \int_\Omega \left(\phi^D - \bar{\phi}\right) d\boldsymbol{x} \\ s.t. & \phi^- \leq \phi^D \leq \phi^+ \end{array} \tag{2.14}$$

Equation (2.14) constitutes the constrained deconvolution method to ensure boundedness and conservation. In the following, the solution to this optimization problem is referred to as regularized deconvolution method (RDM).

To used the model in LES efficiently, the deconvolution is first conducted using the Wiener filter, Eq. (2.10). This is to take advantage of the simplicity of the Wiener filter which is a pre-computed linear operator hence the cost of deconvolution is low. A check for the boundedness and conservation in consequently done over the deconvolved scalar field. Points where any of these two constraints are violated are grouped to form a subset of total points in the simulation, and RDM is applied to this subset of points. The solution from RDM is used to update the initially deconvolved scalars obtained from the Wiener filtering. This approach minimizes the computational cost of deconvolution while preserving the property of boundedness and conservation.

3. DNS setup and results

In the following, we will examine the performance of RDM. For this, we consider direct numerical simulations of a partially-premixed flame in decaying turbulence. The computational setup is schematically shown in Figure 3(a). The configuration used in the simulations is a cubic box with length 1 cm and 256 mesh points along each direction. Periodic boundary conditions are applied in each direction. The turbulence is initialized using the von Karman-Pao energy spectrum with energetic length scale of 1 cm and turbulent Reynolds number of $Re_\tau = 100$. The Kolmogorov length scale is $\eta \approx 1$ μm. In the current configuration, the eddy-turnover time scale is $\tau_\mathrm{u} = 1$ ms, which is used as the reference for non-dimensionalization.

The reaction chemistry is described by a three step skeletal methane mechanism (Dryer & Glassman 1972; Westbrook & Dryer 1971). By considering a partially premixed flame configuration, the initial condition is constructed from solutions of a three-stream flamelet model (Ihme & See 2011), where Z is the mixture fraction and W is defined as the oxidizer splitting parameter, as shown in Figure 3(b). The species and temperature are obtained by mapping the profile of Z and W in Figure 3(a) on the flamelet solutions. With this definition, the oxidizer at $Z = 0$ is constructed using an inhomogeneous mixture of two streams. The state at $W = 0$, $Z = 0$ has a mixture composition of air, with $Y_{\mathrm{O}_2} = 0.23$, $Y_{\mathrm{N}_2} = 0.77$ and $T = 300$ K. The mixture composition at $W = 1$, $Z = 0$ is consist of $Y_{\mathrm{O}_2} = 0.09$, $Y_{\mathrm{N}_2} = 0.91$ and temperature $T = 1400$ K, and the state at $W = 0$, $Z = 1$

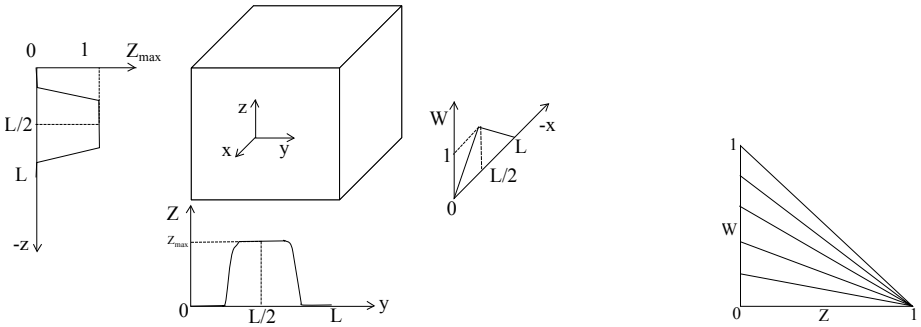

(a) (b)

FIGURE 3. DNS configuration of a partial-premixed flame: (a) geometry with scalar initialization profile; (b) three stream mixture fraction and definition of oxidizer split.

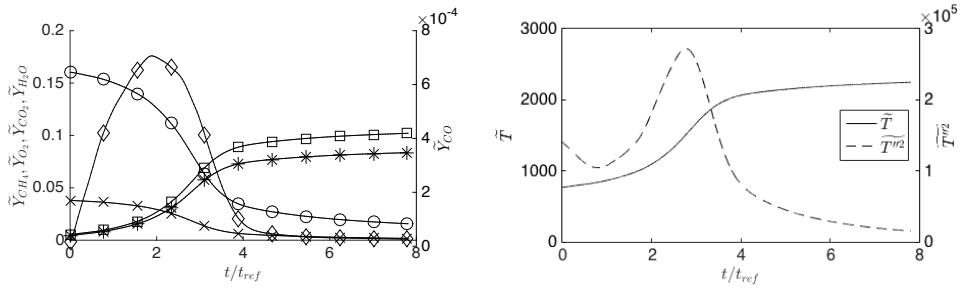

(a) (b)

FIGURE 4. Scalar profiles: (a) mass fraction of reactive species: CH_4 ($\times$), O_2 ($\bigcirc$), CO ($\diamond$), CO_2 ($\square$), H_2O ($*$); (b) mean and variance of temperature.

refers to the fuel stream consisting of pure methane. The scalars are initialized from flamelet solutions at $\chi_{st} = 5\ \mathrm{s}^{-1}$, which is close to the extinction point for all values of oxidizer split. W and Z are stratified in x and y direction respectively, as shown by the profiles in Figure 3(a). The shear layer thickness δ_s in this setup is evaluated as 1 mm, following the definition

$$\delta_s = \left(\frac{1}{|\nabla Z|}\right)_{Z=Z_{st}}. \tag{3.1}$$

Figure 4(a) and Figure 4(b) show species mass fractions and temperature profiles over eight eddy-turnover time. It is seen that the flame reaches equilibrium in around five eddy-turnover times. The peak heat release rate is observed at around three eddy-turnover times.

4. A priori analysis

Results shown in the *a priori* study consider the instantaneous flow field at $t/\tau_{\mathrm{u}} = 3$, where a maximum heat release rate is observed. In the following analysis, the scalars are filtered using a box filter with specified filter width of Δ/δ_s, both the performance of ADM and RDM are investigated over a range of filter widths.

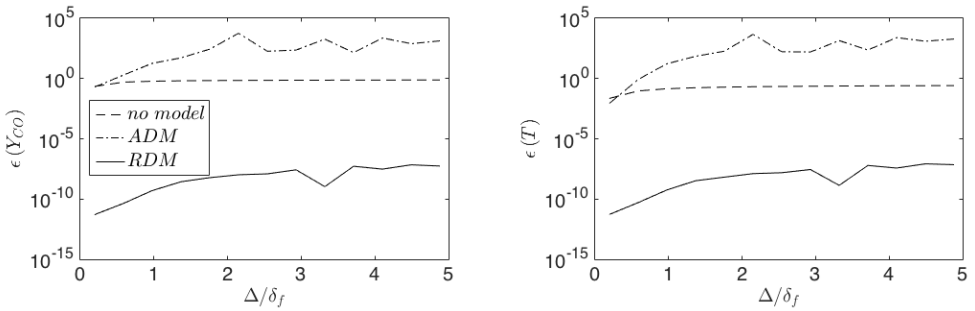

(a) CO-mass fraction (b) Temperature

FIGURE 5. Normalized error in scalars comparing different deconvolution closures.

4.1. *Deconvolution and scalar reconstruction*

4.1.1. *Scalar reconstruction error*

The normalized scalar reconstruction error is defined as

$$\epsilon\,(\phi) = \|\phi - \phi^D\|_2 / \|\phi\|_2\,. \tag{4.1}$$

The reconstruction error is plotted as a function of filter width, normalized by the shear layer thickness, for different deconvolution models in Figure 5. As a general trend for all models, the scalar reconstruction error increases with filter width, and this property is independent of the type of scalars. For cases without deconvolution model applied, the error becomes of order unity. Using ADM (dotted lines), the error reduces for the case with filter width lower than one fifth of the flame thickness. As the filter width increases, the error for the reconstructed scalars using ADM exceeds the error without deconvolution. In comparison, scalars that are reconstructed by RDM have an normalized error lower than 10^{-5} for all filter widths.

Noticed that all reconstructed scalars behave similarly for each deconvolution method, only results for the CO-mass fraction are shown in the following analysis.

A comparison of reconstructed flow field results is show in Figure 6 using Favre filtering with filter width $\Delta/\delta_s = \{0.2\ 1.0\ 2.0\}$. The first column shows an unfiltered CO-mass fraction contour. The second column shows the filtered CO-mass fraction for three test filter widths. It is observed that the small-scale structure is filtered out as the filter width increases. The third and fourth columns show the reconstructed CO-mass fraction using ADM and RDM, respectively. With $\Delta = \delta_s$, both methods provides comparable results. However, as the filter width increases, the flame structure reconstructed using ADM becomes corrupted by spurious oscillations. In regions adjacent to the flame, regimes with negative CO-mass fraction are observed. In contrast, the flame structure is preserved using RDM for all three filter widths.

4.1.2. *Spectral content*

Figure 7 compares the energy spectrum of CO-mass fraction reconstructed using different methods for cases with filter width $\Delta/\delta_s = \{0.2\ 1.0\ 2.0\}$. Filtered CO-mass fraction without deconvolution shows an increase in energy loss as the filter width increases, starting with high wave number. With ADM, the energy spectrum is restored for the case $\Delta = 0.2\delta_s$, with slight over-amplification at high wave numbers. The degree of over-amplification grows with increasing filter width, and the wave number where the

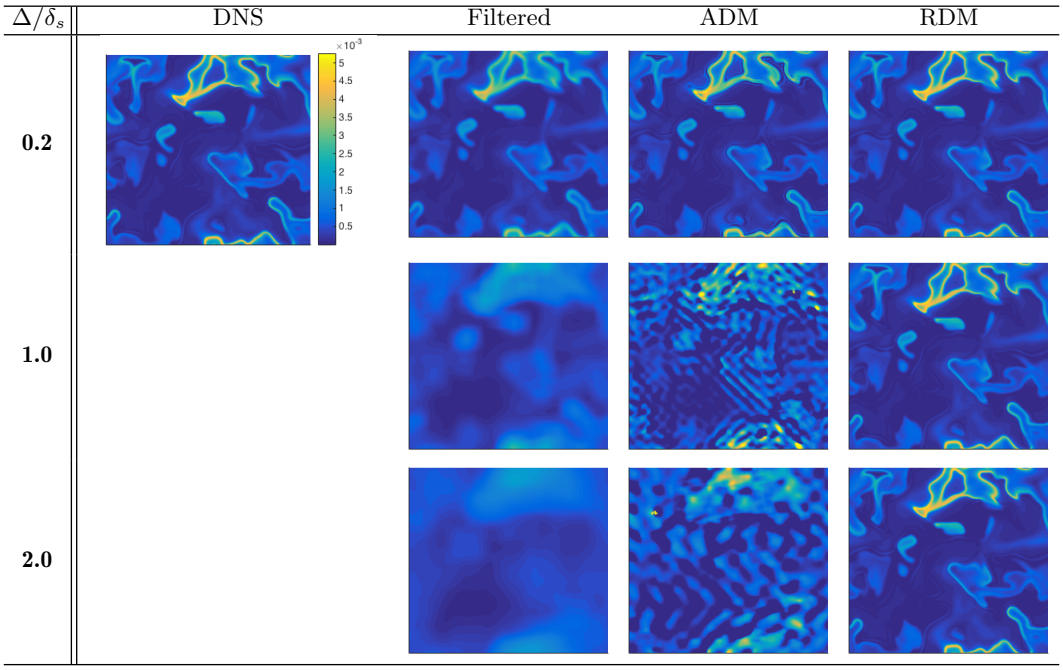

FIGURE 6. CO-mass fraction reconstructed using ADM and RDM for different filter width.

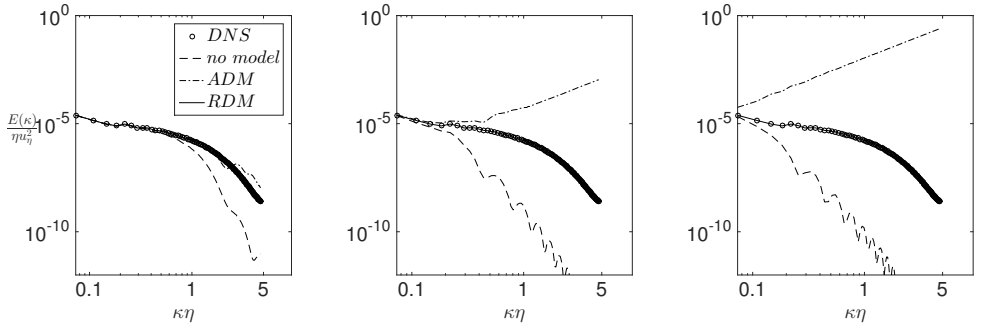

(a) $\Delta/\delta_s = 0.2$ (b) $\Delta/\delta_s = 1.0$ (c) $\Delta/\delta_s = 2.0$

FIGURE 7. Spectrum of CO mass fraction $\hat{Y}_{\mathrm{CO}}$ for DNS (circles, o), no deconvolution method (dashed lines, –), ADM (dash dotted lines, -.), RDM (solid lines, -).

over-amplification starts gets reduced. This result explains the observation of the growth of the error with filter width in scalar reconstruction using ADM. In contrast, a match of energy spectrum with DNS is observed for cases using RDM over all filter widths.

Results for scalar reconstruction using RDM show that the method is stable for all filter widths. The fine-scale flame structure is recovered after RDM deconvolution.

4.2. *Turbulent chemical source term in LES equation*

In finite rate chemistry, the chemical source term is a function of the mass fraction of the reactive scalars and temperature, which is $\rho\dot{\omega}(\phi)$, with $\phi = T$ & Y_i, $i = 1, ..., N$, where Y_i is the species mass fraction. In LES, the chemical source term is filtered, $\overline{\rho\dot{\omega}}(\phi)$. With the deconvolution model, scalars are reconstructed from the filtered ones that are solved

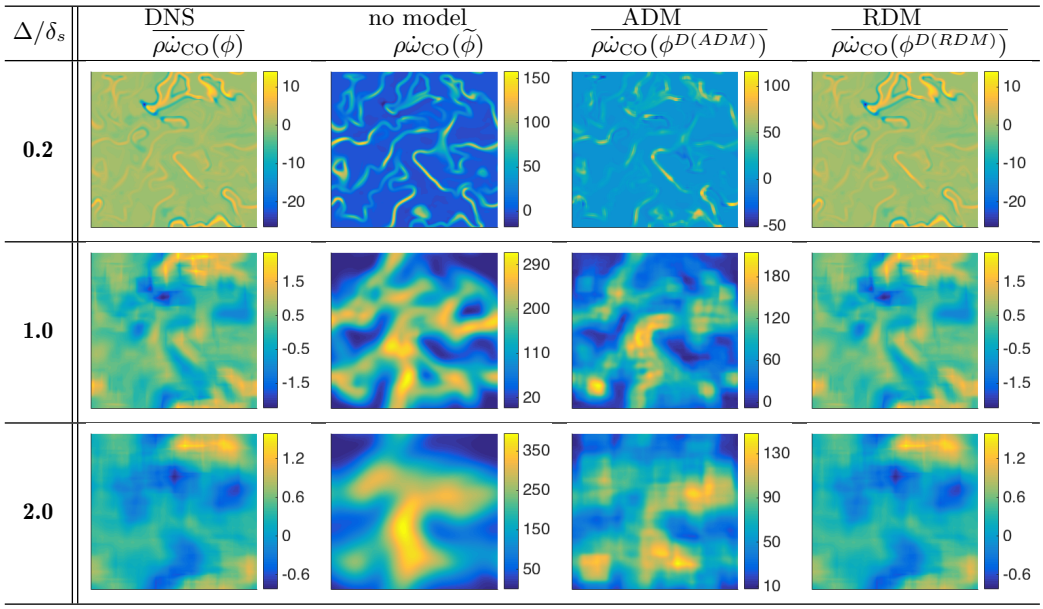

FIGURE 8. Chemical source term $\overline{\rho\dot{\omega}}_{\mathrm{CO}}$ with different filter width computed using ADM and RDM.

as variables in LES transport equations. The deconvolved scalars ϕ^D can be used as an approximation to the fully resolved scalars, ϕ. Therefore, the closure to the turbulent chemical source term using deconvolution model can be computed as $\overline{\rho\dot{\omega}}(\phi^D)$.

Figure 8 shows the turbulent chemical source term of CO as a function of filter width Δ. With increasing Δ, the flame structure is filtered out. The chemical source term computed using filtered scalars directly lead to an over-prediction. In addition, when Δ exceeds δ_s, the topology of the flame is mis-predicted. The ADM method tends to reduce the over-prediction of the chemical source term by a factor of two, but the result is still two orders of magnitude larger than the DNS result. The flame topology obtained using ADM follows the filtered results, which is uncorrelated with the original flame topology. In contrast, the chemical source term computed using RDM matches the DNS results qualitatively.

Figure 9 shows quantitative comparisons of the chemical source term with filter width equals to δ_s. Without deconvolution method applied (Figure 9(a)), $\overline{\rho\dot{\omega}}$ is biased towards being over-predicted. The scattering near the regression line indicates that the variance of the prediction is significant. With ADM, no improvement over the prediction is observed, as shown in Figure 9(b). This is due to the over-amplification of scalars starting at the middle range of the wave number. In Figure 9(c) it is found that all scatter points coincide with the regression line, indicating that RDM provides an unbiased prediction of the chemical source term.

5. Conclusions

In this paper, a new deconvolution method for reactive scalars is proposed. The proposed regularized deconvolution method addressed drawbacks of existing linear deconvolution methods by ensuring boundedness and conservation of scalars.

An *a priori* analysis is conducted to examine the performance of RDM by considering a

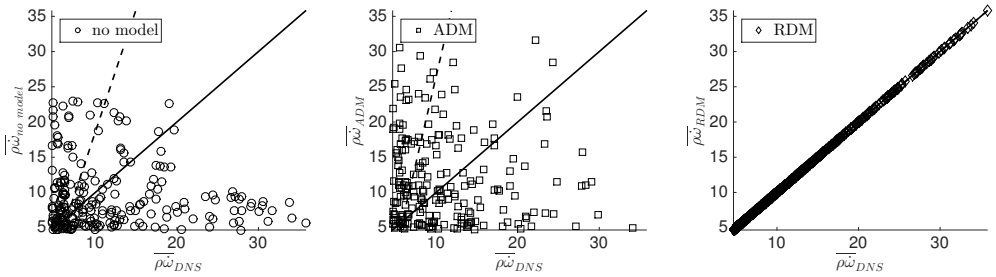

(a) no model (b) ADM (c) RDM

FIGURE 9. Turbulent chemical source term comparison between DNS and reconstruction using different deconvolution methods.

partially premixed flame configuration. High accuracy and stable performance for scalar reconstruction are observed using RDM. The filtered chemical source term and scalars that are correctly predicted from RDM are shown to preserve the flame topology. Future steps consider the application of this method in LES.

REFERENCES

COLEMAN, T. & LI, Y. 1996 A reflective newton method for minimizing a quadratic function subject to bounds on some of the variabLES. *SIAM J. Optimization* **16**, 1040–1058.

DOMINGO, P. & VERVISCH, L. 2015 Large eddy simulation of premixed turbulent combustion using approximate deconvolution and explicit flame filtering. *Proc. Combust. Inst.* **35** (2), 1349–1357.

DRYER, F. & GLASSMAN, I. 1972 High-temperature oxidation of co and ch. *Proc. Combust. Inst.* **14** (1), 987–1003.

FIORINA, B., VICQUELIN, R., AUZILLON, P., DARABIHA, N., GICQUEL, O. & VEYNANTE, D. 2009 A filtered tabulated chemistry model for LES of premixed combustion. *Combust. Flame* **157** (3), 465–475.

GICQUEL, O., DARABIHA, N. & DOMINIQUE, T. 2000 Laminar premixed hydrogen/air counterflow flame simulations using flame prolongation of ILDM with differential diffusion. *Proc. Combust. Inst.* **28**, 1901–1908.

IHME, M., CHA, C. & PITSCH, H. 2005 Prediction of local extinction and re-ignition effects in non-premixed turbulent combustion using a flamelet/progress variable approach. *Proc. Combust. Inst.* **30** (1), 793–800.

IHME, M. & SEE, Y. 2011 LES flamelet modeling of a three-stream mild combustor: Analysis of flame sensitivity to scalar inflow conditions. *Proc. Combust. Inst.* **33** (1), 1309–1317.

KERSTEIN, A. 1988 A linear-eddy model of turbulent scalar transport and mixing. *Combust. Sci. Tech.* **60** (4-6), 391–421.

LAYTON, W. & REBHOLZ, L. 2012 *Approximate Deconvolution Models of Turbulence: Analysis, Phenomenology and Numerical Analysis*. Berlin Heidelberg: Springer.

MELLADO, J., SARKAR, S. & PANTANO, C. 2003 Reconstruction sub-grid models for nonpremixed combustion. *Phys. Fluids* **15** (11), 3280–3307.

OIJEN, J. & GOEY, L. 2000 Modeling of premixed laminar flames using flamelet generated manifolds. *Combust. Sci. Tech.* **161** (1), 113–137.

Pantano, C. & Sarkar, S. 2001 A surged model for nonlinear functions of a scalar. *Phys. Fluids* **13** (12), 3803–3819.

Pierce, C. & Moin, P. 2004 Progress-variable approach for large-eddy simulation of non-premixed turbulent combustion. *J. Fluid Mech.* **504**, 79–97.

Pope, S. 1985 PDF methods for turbulent reactive flows. *Prog. Energy Combust. Sci.* **11**, 119–192.

Schlatter, P., Stolz, S. & Kleiser, L. 2004 LES of transitional flows using the approximate deconvolution model. *Inter. J. Heat and Fluid Flow* **25** (3), 549–558.

Stolz, S., Adams, N. & Kleiser, L. 2001*a* An approximate deconvolution model for large-eddy simulation with application to incompressible wall-bounded flows. *Phys. Fluids* **13** (4), 997–1015.

Stolz, S., Adams, N. & Kleiser, L. 2001*b* The approximate deconvolution model for large-eddy simulations of compressible flows and its application to shock-turbulent-boundary-layer interaction. *Phys. Fluids* **13** (10), 2985–3001.

Stolz, S. & Adams, N. A. 1999 An approximate deconvolution procedure for large-eddy simulation. *Phys. Fluids* **11**, 1699–1701.

Westbrook, C. & Dryer, F. 1971 Simplified reaction mechanisms for the oxidation of hydrocarbon fuels in flames. *Combust. Sci. Tech.* **27** (1-2), 31–43.

Wu, H., See, Y., Wang, Q. & Ihme, M. 2015 A pareto-efficient combustion modeling framework for predicting complex flame configurations. *Combust. Flame* **162**, 4208–4230.